ACTUATORS

Micrometer-sized electrically programmable shape-memory actuators for low-power microrobotics

Qingkun Liu[1]*, Wei Wang[1,2], Michael F. Reynolds[1], Michael C. Cao[3], Marc Z. Miskin[4], Tomas A. Arias[1], David A. Muller[3,5], Paul L. McEuen[1,5]*, Itai Cohen[1,5]*

Shape-memory actuators allow machines ranging from robots to medical implants to hold their form without continuous power, a feature especially advantageous for situations where these devices are untethered and power is limited. Although previous work has demonstrated shape-memory actuators using polymers, alloys, and ceramics, the need for micrometer-scale electro–shape-memory actuators remains largely unmet, especially ones that can be driven by standard electronics (~1 volt). Here, we report on a new class of fast, high-curvature, low-voltage, reconfigurable, micrometer-scale shape-memory actuators. They function by the electrochemical oxidation/reduction of a platinum surface, creating a strain in the oxidized layer that causes bending. They bend to the smallest radius of curvature of any electrically controlled microactuator (~500 nanometers), are fast (<100-millisecond operation), and operate inside the electrochemical window of water, avoiding bubble generation associated with oxygen evolution. We demonstrate that these shape-memory actuators can be used to create basic electrically reconfigurable microscale robot elements including actuating surfaces, origami-based three-dimensional shapes, morphing metamaterials, and mechanical memory elements. Our shape-memory actuators have the potential to enable the realization of adaptive microscale structures, bio-implantable devices, and microscopic robots.

INTRODUCTION

Shape-memory effect refers to the ability of certain materials to hold a temporary shape and recover their original shape upon exposure to an external stimulus such as temperature (*1*), electric field (*2*), magnetic field (*3*), or light (*4*). An ideal shape-memory actuator that can be integrated into microscopic intelligent systems has several challenging requirements: the material should be able to hold its form for a long time (from several hours to months), be electrically actuated, and be bendable to micrometer-scale radii of curvature. The actuator should operate at fast time scales, be robust, and be reproducible. In addition, it should be manufactured using techniques consistent with modern semiconductor fabrication to enable integration with the existing electronics. Figure 1A and table S1 summarize the state of the art of electrically bendable actuators. Although there are many systems for volatile actuation (borderless shaded regions) with some examples even at the microscale, much less progress has been made in developing shape-memory materials (shaded regions with black border) at the microscale. For example, electrothermal shape-memory polymers (*5*) and alloys (*6*) tend to have small bending curvatures, large working voltages, and specialized fabrication requirements (*7*–*9*). A more promising approach using electrochemically induced actuation meets the requirement of low working voltages (<10 V) and has been demonstrated using a variety of materials, such as metals (*10*, *11*), ionic liquid gels (*12*), and conductive polymers (*13*), but the shape-memory effect in these systems remains largely elusive. Recently, it has been shown that silicon nanoscaffolds can maintain an actuated state by driving lithium ions into the silicon and trapping them (blue circle) (*14*). Even with this system, however, operation is slow and cyclability is limited. Here, we show that a different electrochemical strategy—using the surface oxidation of thin platinum metal films—creates electrically controlled shape-memory actuators with high cyclability that respond quickly and reach submicrometer bending radii (Fig. 1A, top left, and Movie 1).

RESULTS

The starting point for this work is the surface electrochemical actuator (SEA) platform recently introduced by our group (*10*). The device consists of a nanometer-thick platinum thin film capped on one side by a passive layer. The platinum is grown via atomic layer deposition (ALD), and the ones reported here are 7 nm thick and capped on one side by a 2-nm-thick layer of either sputtered titanium or ALD titanium dioxide, which produces even higher curvatures (Fig. 1B). The ALD of continuous, nanometer-thin layers is crucial to achieving an ultrasmall bending radius and high durability.

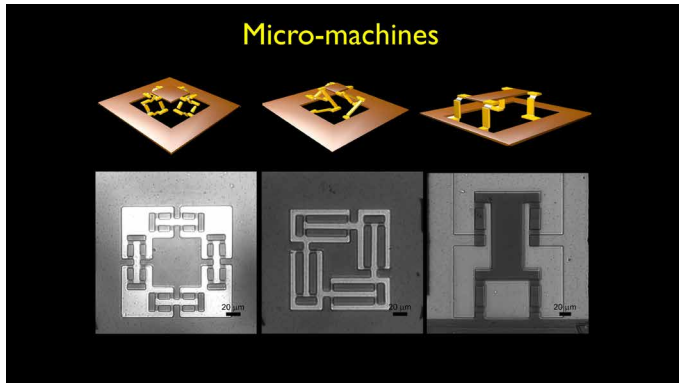

Movie 1. Micrometer-sized electrically driven shape-memory actuators for microscopic robotics.

[1]Laboratory of Atomic and Solid-State Physics, Cornell University, Ithaca, NY 14853, USA. [2]Sibley School of Mechanical and Aerospace Engineering, Cornell University, Ithaca, NY 14853, USA. [3]School of Applied and Engineering Physics, Cornell University, Ithaca, NY 14853, USA. [4]Department of Electrical and Systems Engineering, University of Pennsylvania, Philadelphia, PA, USA. [5]Kavli Institute at Cornell for Nanoscale Science, Cornell University, Ithaca, NY 14853, USA.
*Corresponding author. Email: ql59@cornell.edu (Q.L.); plm23@cornell.edu (P.L.M.); itai.cohen@cornell.edu (I.C.)

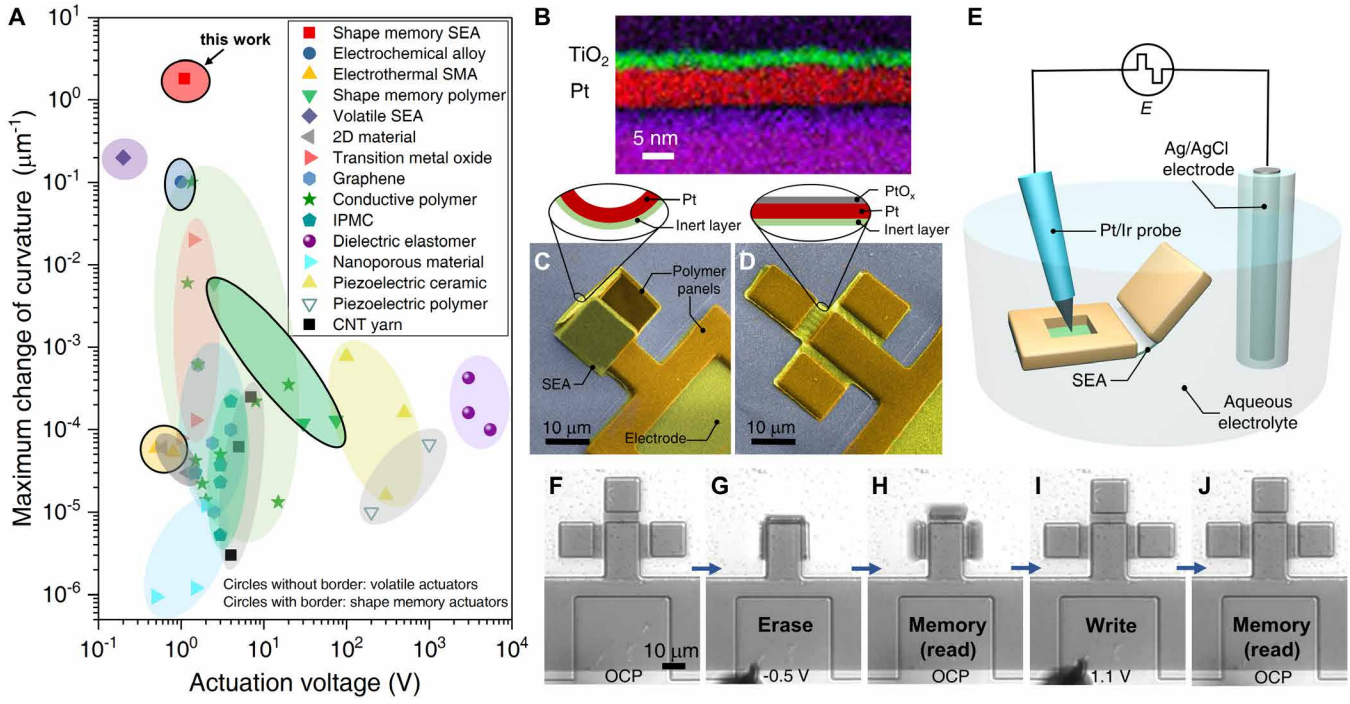

Fig. 1. Shape-memory SEAs: Composition, structure, and basic operation. (**A**) Literature survey of the performance of voltage-driven bendable actuators. The regions with black borders show shape-memory actuators, and the regions without black borders show shape-change actuators without memory. (**B**) A false-color TEM image of a SEA cross section: 7 nm of platinum (red) capped on one side by a 2-nm TiO_2 film (green) grown on the silicon wafer (magenta). (**C**) A false-color SEM image of a SEA microgripper that has been set to the reduced state and then removed from solution via critical point drying. In the reduced state, SEAs are bent away from the inert layer. (**D**) A false-color SEM image of a SEA microgripper that has been set to the oxidized state and then removed from solution via critical point drying. The platinum oxide causes the microgripper to flatten. The insets of (C) and (D) show a cross-sectional schematic of the SEA hinge in the reduced and oxidized states, respectively. The SEA hinge holds each of these states even when the voltage is removed from the device. (**E**) Schematic of the experiment. SEAs are patterned with panels to define hinges. We apply a voltage to the actuator with a platinum/iridium probe versus a distant Ag/AgCl electrode, causing the actuator to bend. (**F** to **J**) Optical micrographs showing a SEA microgripper in action. (F) The SEA microgripper starts in the oxidized state. (G) We then apply −0.5 V versus Ag/AgCl to reduce it, causing the panels to curve up. (H) When we remove the probe, the SEA hinge remains in the reduced curved state under the OCP. (I) We oxidize the SEA hinge again by applying 1.1 V versus Ag/AgCl, causing the SEA hinge to flatten. (J) The SEA hinge remains in the oxidized, flat state when we remove the probe.

Transmission electron microscopy (TEM) images show that the platinum is polycrystalline with domain sizes of ~10 nm, and the protective capping layer is highly amorphous and conformally caps the platinum layer (Fig. 1B and fig. S1). The small sizes and random orientations of the crystalline domains in the platinum ensure isotropic expansion and contraction of the actuator. By patterning 1-μm-thick rigid polymeric panels on top of the actuators, we localize bending to the unpatterned region and produce what are effectively folds (Fig. 1, C and D, and fig. S2) (*15*, *16*).

We demonstrate that shape memory can be induced in SEAs in phosphate-buffered saline (PBS; 1×; pH 7.45) through the electrochemical oxidation of the exposed platinum surface at larger positive applied voltages. This mechanism is distinct from the volatile operation of SEAs via adsorption/desorption of oxygen or hydrogen species on the surface, which we described in our previous work (*10*). Oxidizing the platinum causes it to expand and bend the whole actuator. This process is shown in Fig. 1 (C and D). A voltage is applied to the actuator versus a reference electrode (typically Ag/AgCl in 3 M KCl), as shown in Fig. 1E. Figure 1C shows a SEA in the reduced state: The SEA is bent away from the inert layer due to the prestress between the Pt layer and the inert capping layer. Figure 1D shows an oxidized SEA: The SEA flattens due to the expansion of platinum oxide at the exposed surface.

SEAs have stable states with and without the platinum oxide layer even if the voltage is removed, i.e., shape memory. The shape-memory "read," "write," and "erase" operations of a simple SEA gripper are shown in Fig. 1 (F to J). The microgripper consists of SEA hinges linking 10 μm–by–10 μm rigid panels. In the oxidized state, the SEA hinges are flat and the gripper is open (Fig. 1F). To erase the state, a voltage of −0.5 V was applied to the SEA relative to the Ag/AgCl reference electrode that caused the gripper to change into the closed position (Fig. 1G). To read the state, we lifted the voltage probe and observed the bending state of the device at its open circuit potential (OCP) in the microscope. Between Fig. 1G and Fig. 1H, the gripper relaxes slightly. For the pH 7.45 conditions reported here, removing the probe resulted in an effective OCP of about 0.3 to 0.4 V, at which the reduced platinum surface quickly adsorbs a monolayer of O^{2-}/OH^- ions, causing the platinum surface to expand slightly and relax the actuator. To write the original state again, a voltage of 1.1 V was used to return the gripper to the open position (Fig. 1, I and J). A video of the process can be seen in movie S1. This shape-memory operation can be repeated hundreds of times.

Figure 2A further illustrates the electrochemical mechanism behind the shape-memory operation. Low voltages cause reversible electrochemical adsorption of O^{2-}/OH^- ions decomposed from the water onto the Pt (states I and II in Fig. 2A) (*10*). At higher positive

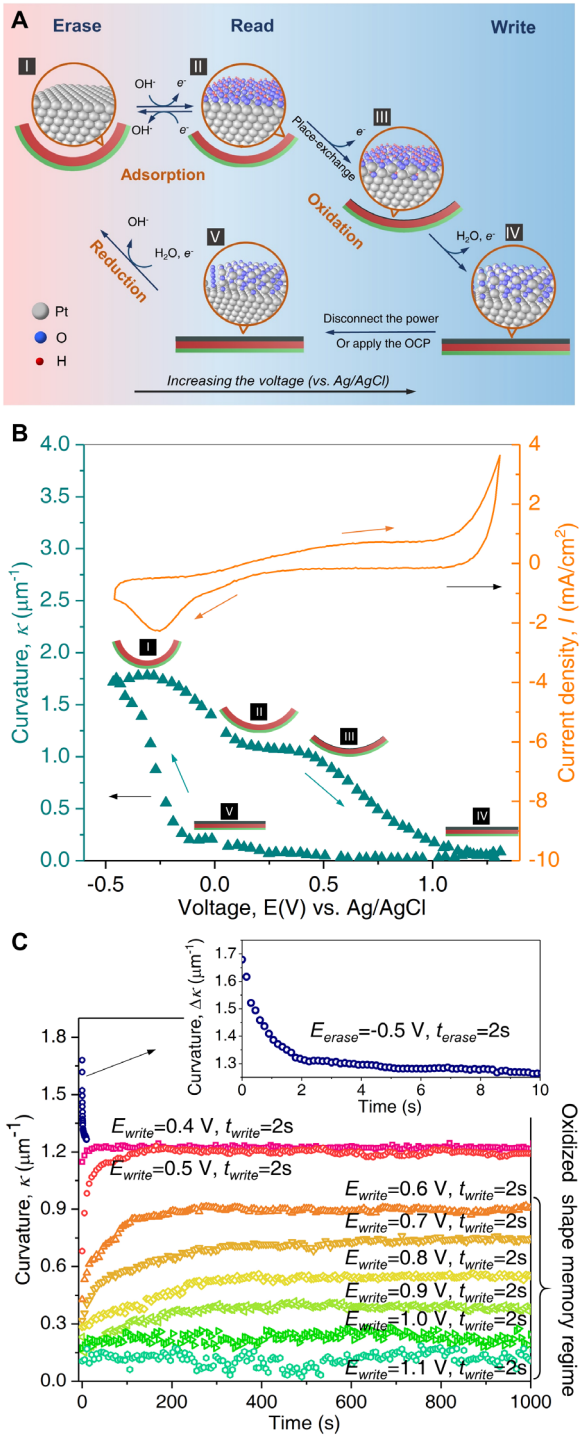

Fig. 2. Electrochemistry of actuation and memory. (**A**) Schematic of the electrochemical processes. There is a volatile regime (states I and II) associated with O^{2-}/OH^- adsorption/desorption at lower voltages and a shape-memory regime (from states II to IV and from states V to I) associated with nonvolatile oxidation and reduction of the platinum over a broader voltage range. Red layer, Pt; green layer, inert layer; black layer, PtO_x. (**B**) In situ characterization of the cyclic voltammetry and bending curvature versus applied voltage at a sweep rate of 1 V/s. The schematic insets illustrate the state of the actuator, with Roman numerals indicating the corresponding states in the electrochemistry schematic. (**C**) The curvature of the SEA varies with time when the SEA is oxidized at different voltages for 2 s and disconnected from the power source. The stable saturation state at a curvature of 1.2 μm^{-1} corresponds to rapid ion equilibration at the platinum surface as O^{2-}/OH^- desorbs (top two curves) under the OCP ~0.3 to 0.4 V. The other stable saturation states corresponding to the oxidized shape-memory regime stem from the different thicknesses of the platinum oxide layers that develop under application of higher voltages from 0.6 to 1.1 V. Inset: The curvature relaxes quickly from 1.7 to 1.2 μm^{-1} after disconnecting from the erasing signal. The error in each panel is on the order of the symbol size.

writing voltages, the initial O^{2-} adatoms undergo an interfacial place-exchange process with the Pt surface atoms, leading to a quasi–three-dimensional (3D) surface lattice (*17*), and finally exchange with the deeper Pt ions to form a nanometer-thick nonstoichiometric oxide PtO_x (states III and IV in Fig. 2A). Unlike adsorption of ions onto the surface at low voltages, this oxidation process is irreversible within a finite electrochemical window over the time scales of hours, well beyond that needed for many applications. Consistent with this observation, the cyclic voltammetry shows that there is a separation of ~1 V between the oxidation plateau and the reduction peak (the top curve in Fig. 2B). Figure 2B and fig. S3 show the curvature of the actuator measured during this process (movie S2). A large hysteresis is observed over the range +1.3 to −0.4 V, due to the stresses created by the chemically irreversible growth and reduction of platinum oxide.

When the probe was disconnected from a SEA after oxidation (the read state), the actuator retained its curvature due to the stable oxide layer, as shown in Fig. 2C. To obtain these data, we began with the device in the fully reduced state, applied a constant oxidizing voltage for 2 s, disconnected the device, and measured its curvature versus time. For voltages lower than 0.5 V, the device curvature relaxed to 1.2 μm^{-1} over a time scale of seconds, indicating that no substantial oxidation had occurred. For larger applied voltages, the device curvature saturated at a fixed value that depended on the applied voltage and writing time. The SEA can therefore hold multiple curvatures associated with different amounts of oxidation. These curvatures were maintained over time scales longer than hours (figs. S4 and S5). We hypothesize that the slow relaxation of the curvature over time is due to oxygen ions escaping slowly from the surface of PtO_x at domain boundaries and defects where energy barriers are lower. The relaxation time scale could be a function of environmental conditions including temperature and pH. A subsequent negative "erasing" voltage could be used to rapidly remove this oxide, returning the actuator to its unoxidized state. Thus, Pt oxidation/reduction drives the reconfigurable operation of the SEAs.

The writing/erasing operations, switching speed, and cycling stability of a SEA are shown in Fig. 3. Figure 3A shows rapid switching between the oxidized and reduced states using brief electrical pulses of 1.1 and −0.5 V, respectively, a process reminiscent of writing/erasing electronic states in a nonvolatile information storage device. Switching between these states was very fast, as shown in Fig. 3B. The actuator returned to the completely reduced state in less than 20 ms, a time scale that depends on actuator dimensions and is consistent with fluid drag limited motion. The oxidation process was slower (Fig. 3B), but with the most rapid change still occurring in less than 100 ms. SEA oxidation/reduction was highly repeatable, with only a 5% variation in the oxidized/reduced states after ~100 cycles of operation (Fig. 3, C and D). We have measured the actuation amplitude for a larger number of cycles and have shown that the decrease in amplitude begins to saturate after about 2000 cycles (fig. S6). The actuators have the highest curvatures over the first ~100 cycles and more stable actuation at lower curvature values after several thousand cycles. The reduced cyclability may result from formation of defects or an increase in porosity of the platinum

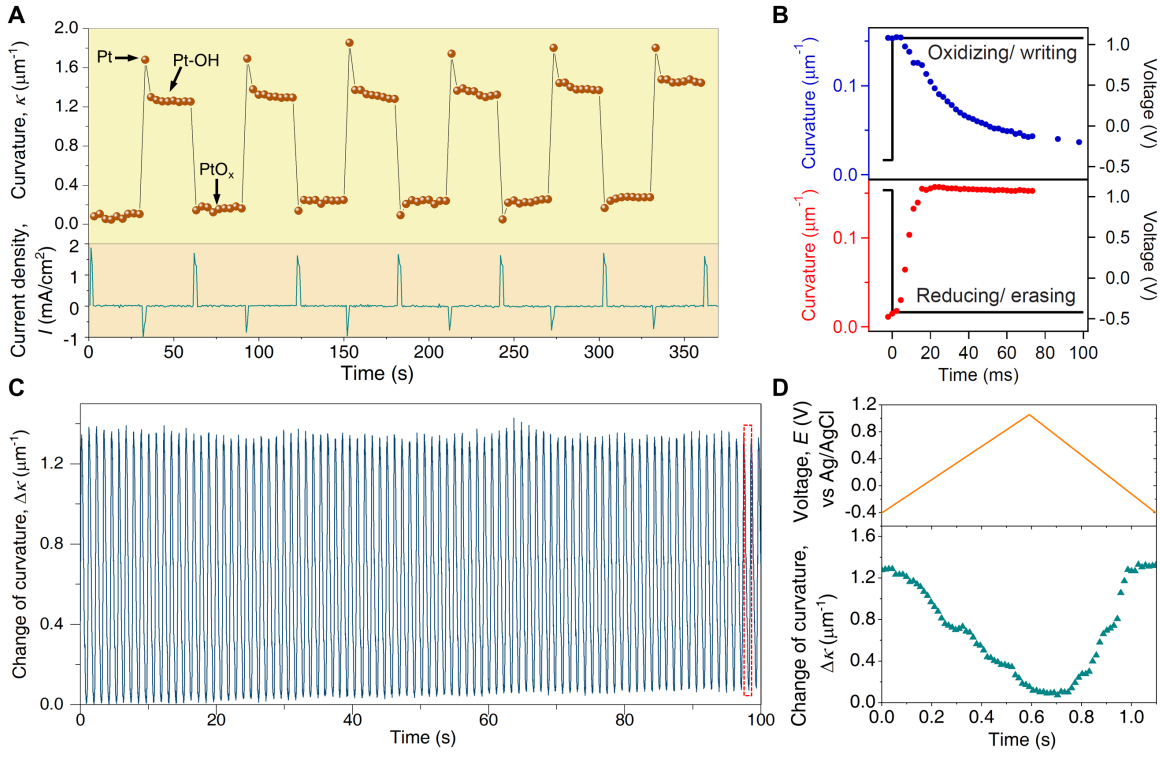

Fig. 3. Electrically programmable memory, switching speed, and cycling stability. (**A**) The bending curvature of a SEA hinge (top) is toggled between the reduced and oxidized shape-memory states via short writing (1.1 V) and erasing (−0.5 V) pulses (bottom). (**B**) Normalized curvature of a Pt/Ti SEA hinge versus time. We find that the curvature switches on a time scale of ~50 ms during the oxidation of the platinum with slow continued change in curvature after that. We find an even faster switching time of ~10 ms during the reduction of the platinum. (**C**) SEA hinge curvature versus number of actuation cycles with an applied voltage sweep of −0.4 to 1.05 V at a frequency of 1 Hz. (**D**) The applied voltage and resulting curvature change versus time for the cycle highlighted by the red dashed rectangle in (C). We find that SEA can be cycled over 100 times with only a 5% variation in the curvature amplitude. The error in each panel is on the order of the symbol size.

film. Such effects will be important to investigate in future work. Particularly, one limiting factor of the durability is the electrochemical corrosion of platinum, whose rate depends on the electrolyte, working voltage, etc. During the reduction of the platinum oxide, a small fraction of platinum ions will form soluble Pt^{2+} at the surface of the platinum and dissolve in the electrolyte (*18*). On the basis of the previously reported corrosion rate of platinum of 2 ng/(cyc·cm^2) in 1× PBS solution (*18*), a 10-nm-thick microactuator could cycle 10^4 times before the platinum film dissolves. Collectively, the low-voltage operation, fast writing speed, long-time stability, high cyclability, and small size establish SEAs as a robust technology for implementing electrically driven shape memory at the microscale.

To quantitatively understand the SEA operation, we note that the change in curvature, Δκ, for the SEA hinge is related to the layer thickness h_{ox} of the surface oxide via the Stoney equation (*19*)

$$\Delta\kappa = \frac{6(1-\nu_s)E_{ox}h_{ox}}{E_s h_s^2}\varepsilon_{ox} \quad (1)$$

where ε_{ox}, E_s, E_{ox}, h_s, and ν_s are the strain in the oxide layer, the Young's moduli of the Pt/TiO_2 substrate and oxide layer, and the thickness and Poisson ratio of the Pt/TiO_2 substrate, respectively (see the Supplementary Materials for details). We assume the Young's modulus and Poisson ratio of these materials are the same as the values measured in the bulk, whereas the overall film thicknesses can be estimated from the TEM measurements. Thus, the oxide thickness h_{ox} and strain ε_{ox} are the only unknowns.

To determine h_{ox} for different oxidation conditions, we conducted a separate experiment to measure the in-plane conductivity of ALD platinum thin films during electrochemical oxidation as shown in Fig. 4. Related work has studied oxidation/adsorption (*20*) and strain (*21*) using this approach. Figure 4A shows a thin (about 5 nm) ALD Pt film grown by the same process as the SEA and a schematic of its cross section. The cyclic voltammogram shows the same voltage dependence for oxidation and reduction as the SEA. In addition, the conductance shows the same large hysteresis as the curvature of a SEA. Thus, the oxidation profile in these films should be identical to that in a SEA with the advantage that we can measure the film conductance. The in-plane conductance of this film is shown as a function of the electrochemical potential of the surrounding electrolyte in Fig. 4B. This measurement shows a large decrease in conductance during oxidation of the platinum film, consistent with previous measurements on thin film platinum (*20*). Because platinum oxide has a 10^{-5}-fold smaller conductivity than platinum, the change in conductance is directly proportional to the thickness of the oxidized layer h_{ox}.

Figure 4C shows the inferred oxide layer thickness as a function of time for different oxidizing voltages, using the methods described in the Supplementary Materials. We set the zero of oxide thickness at about −0.3 V versus Ag/AgCl, a potential where the surface is completely reduced but hydrogen adsorption has not yet taken place. At low positive voltages, about 0 to 0.3 V versus Ag/AgCl, we measured a small change in thickness that is steady over time corresponding to the adsorption of oxygen on the platinum surface. At

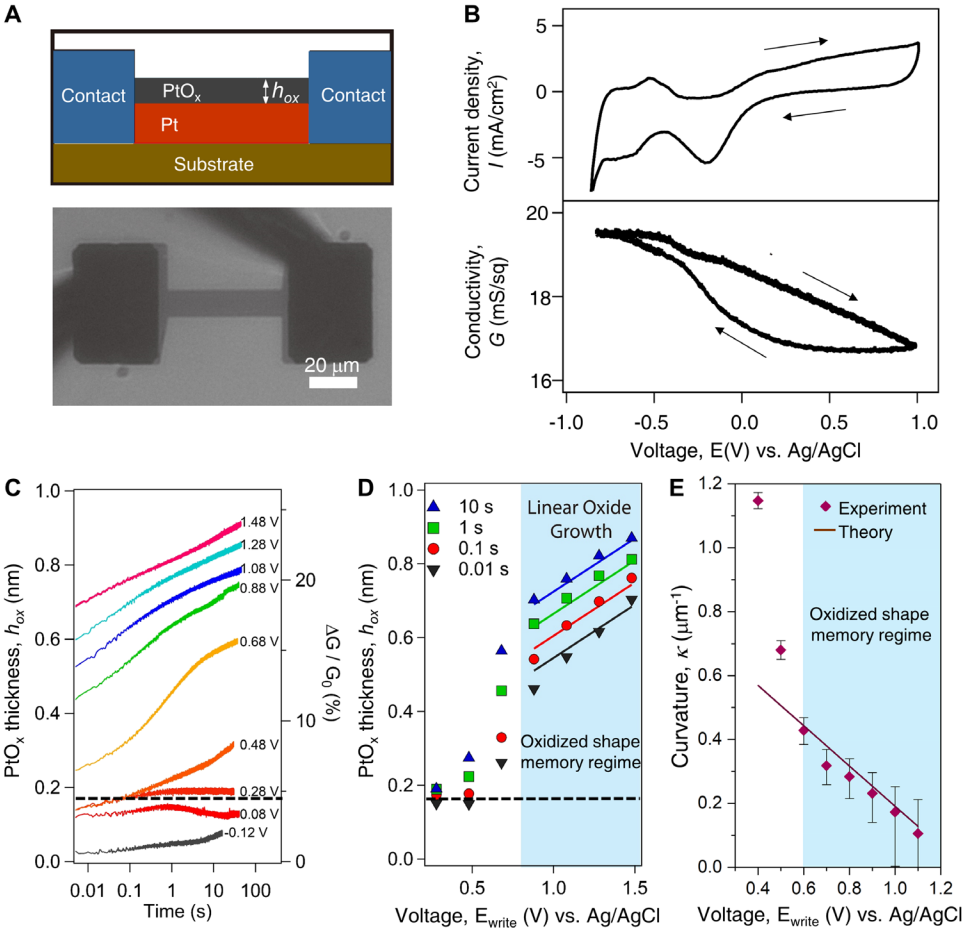

Fig. 4. Electrical measurement of surface oxide layer thickness. (**A**) Top: Cross-sectional schematic of Pt/PtO_x resistor. Bottom: Micrograph of the platinum resistor used to measure conductance as a function of voltage. The dark gray bar in the middle is the atomic layer–deposited platinum, and the black rectangles are thick platinum contacts. Using two probes, we apply a small (<100 mV) source-drain bias across the platinum while sweeping the voltage of the electrolyte versus the platinum with an Ag/AgCl electrode. (**B**) Top: Cyclic voltammogram indicating oxidation and reduction of the film at a sweeping rate of 2 V/s. Bottom: Change in the conductance of the platinum film versus voltage. Conductance at each voltage was determined by measuring current at a small fixed bias across the device. Arrows on the graph indicate the direction of the hysteresis loop. (**C**) Estimated platinum oxide thickness versus log of time for a range of voltages. We used the change in conductance versus time to estimate the thickness of the platinum oxide. For voltages greater than about 0.7 V versus Ag/AgCl, we see linear growth versus log(*t*). (**D**) Estimated platinum oxide thickness as a function of voltage at fixed oxidation times. The dashed lines in (C) and (D) indicate the thickness of adsorbed Pt-OH that exists at the OCP. The solid lines are a fit to the data based on Eq. 2 with the fitting parameters found in the main text. (**E**) Comparison of experimental data for curvature change during the oxidation process with the calculation. The experimental data points are measured after 2 s of oxidation at different voltages. The solid line is the prediction based on Eqs. 1 and 2 in the main text. Here, the prestressed curvature at the reduced state is taken to be 1.68 μm^{-1} (Fig. 2C, inset). We found excellent agreement between the prediction and experimental data for the regime above 0.6 V. (B) to (D) show representative data of the mechanical and electric properties, where the error is on the order of the symbol size. The error in (E) results from manufacturing differences between devices and errors in the measurement of the curvature based on the microscopic images. The curvature measurements are particularly error-prone when the curvature approaches zero.

higher potentials, the oxide thickness grew continuously over time but remained very thin, ~1 nm, even for long growth times, consistent with previous literature (*22*). Above ~0.7 V, the oxide grew approximately logarithmically with time, and the slope on a log *t* scale is relatively insensitive to the voltage in this regime. Figure 4D shows the oxide thicknesses after applying different fixed voltages for the same amount of time. The oxide thickness is linear in voltage above 0.7 V. In this logarithmic regime, we find the oxide thickness (h_{ox}) is approximately given by

$$h_{ox} = h_r\left(\frac{V}{V_0} + \ln\left(\frac{t}{t_0}\right)\right) \quad (2)$$

where $h_r \approx 0.026$ nm, $V_0 \approx 0.09$ V, and t_0 is a fit parameter, $t_0 \approx 5.3 \times 10^{-7}$ s when voltage is referenced to 0 V versus Ag/AgCl.

These results agree with the theory and experiments of Conway *et al.* (*22*), whose place exchange model for oxygen at a platinum interface predicts an equation of the same form as Eq. 2. They disagree with the model of Cabrera and Mott (*23*) and other more recent theories (*24*) where the rate limiter is the escape of Pt ions from the buried Pt/oxide interface, predicting $\frac{1}{h_{ox}} \propto \log\left(\frac{1}{t}\right)$. From Eq. 2, the growth rate for the oxide layer is given by

$$\frac{dh_{ox}}{dt} = \frac{h_r}{t_0} e^{(V/V_0 - h_{ox}/h_r)} \quad (3)$$

This dependence indicates that the growing oxide layer thickness h_{ox} provides an increasing barrier to further growth. Thus, when the applied voltages are low, as is the case in the OCP, a very thin oxide layer is sufficient to markedly slow further oxidation. At higher voltages, oxidation proceeds deeper into the platinum before slowing. Conversely, the oxide film also forms a barrier for reduction of the film in the absence of a reducing voltage, which is why the shape memory is held for such long times (fig. S4). Compared with oxide growth, reduction of the oxide film with a negative voltage versus Ag/AgCl takes place quickly (fig. S7, A and B).

Equations 1 and 2 allow us to design (or write) a desired curvature/oxide thickness on the SEA by selecting an appropriate oxidation time and voltage. The only parameter remaining unknown in Eq. 1 is ε_{ox}. To determine this strain, we used the data from the 0.4- and 1.1-V curves in Fig. 2C and found that $\varepsilon_{ox} \approx 3\%$ for Pt/TiO_2 SEAs. This value is less than but comparable with the relative expansion of PtO_2 compared with Pt of about 10% (*25*, *26*), indicating either an incomplete oxide layer formation or other mechanisms of stress relief besides bending. With this calibration, Eqs. 1 and 2 can be used to determine the curvature for any combination of oxidation voltage and time. We used this approach to calculate the resulting curvature of films that were oxidized for 2 s at different

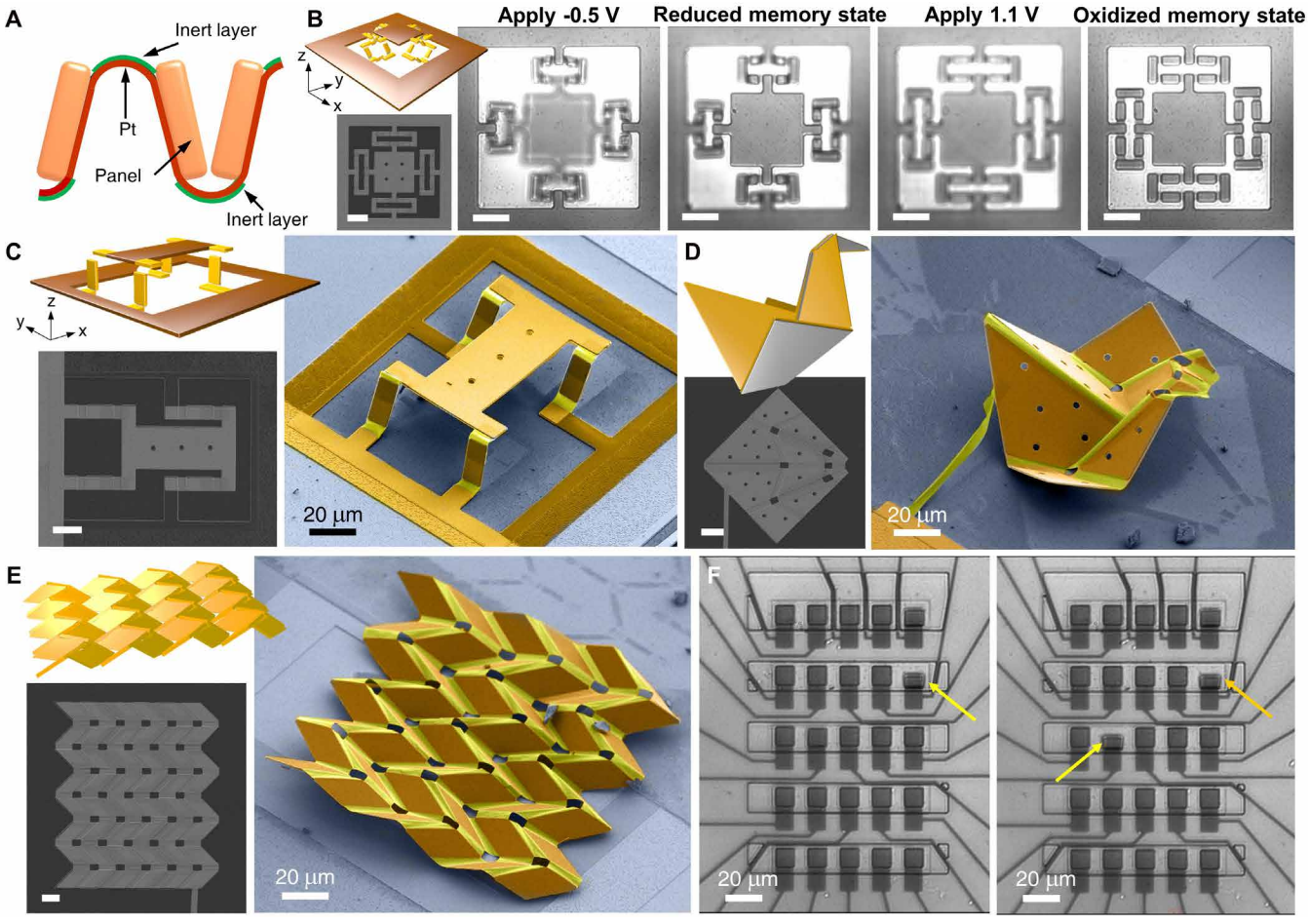

Fig. 5. SEA-enabled multistable micropositioners, origami, metamaterials, and memory arrays. (**A**) The schematic shows the cross section of a bidirectionally folded SEA device defined by the alternating deposition of Pt, inert Ti or TiO_2 layers, and rigid panels. (**B** and **C**) Kirigami-based bistable micropositioner that moves the central stage to a new fixed position and retains its states. (B), along the *z* axis; (C), along the *xz* plane. Optical microscopy image sequence in (B) shows that the device was switched between two bistable states in the PBS (1×, pH 7.45). In (C) to (E), schematics and SEM images of the structure before (grayscale) and after shape-memory actuation (false color) are shown on the top left, bottom left, and right, respectively. Pt/Ti actuators are shown in yellow, and rigid panels are shown in orange. (**D**) Microscale origami duck transforming from a flat sheet and holding its 3D shape. (**E**) Origami-based microscale metamaterial. (**F**) Microscale SEA array that detects a signal and maintains memory of that signal. The image sequence shows that the orange arrow points to a previously actuated shape-memory element, whereas the yellow arrow points to an element undergoing current actuation. Scale bars, 20 μm.

voltages (Fig. 4E). We found excellent agreement between our predictions and the experimental data in the shape-memory regime (above 0.6 V versus Ag/AgCl). The deviation below 0.6 V arises from the fact that the oxygen adsorption at a lower voltage does not obey Eq. 2. In addition, all of the designs in Fig. 5 are based on this quantitative understanding of the relationship between oxidation and curvature.

This predictable behavior allows for the design of microrobotic elements with controlled multistable configurations. SEAs are compatible with standard planar semiconductor fabrication processes, and we can consistently and scalably create complex structures consisting of many actuators. We show a variety of such microscale shape-memory devices in Fig. 5 and movies S3 and S4. These structures use origami- and kirigami-based designs (*27*–*31*) with actuators and rigid panels as shown schematically in Fig. 5A. Mountain and valley folds are dictated by the growth order of the Pt and inert layers and location of the rigid panels using a previously reported approach (*16*). Bidirectional folding creates combinations of mountain (downward) and valley (upward) folds, greatly expanding the space of the shapes compared with unidirectional folding. Microscopic actuating surfaces switching between two stable states are shown in Fig. 5 (B and C) and real-time movie S3. These surfaces are composed of rigid central panels that are actuated by multiple hinges, which act as parallel mechanisms. They have translational strokes of 20 to 30 μm either perpendicular or parallel to the substrates, enabling microstages with 3D motion. Despite being ultrathin, these actuators generate a substantial force. On the basis of beam theory (*19*), a square SEA with a change in curvature of 0.5 μm^{-1}, which is close to the platinum yield strain (*32*–*35*), generates a force of 30 nN at its end (see text SII), allowing the micropositioning stages to carry payloads of 20 to 50 nN. This force is over an order of magnitude higher than those produced by optical traps and about 10,000 times the weight of these devices. Using origami techniques, these shape-memory

actuators can also be used to design complex 3D shapes. In Fig. 5D and real-time movie S4, a classic origami motif is shown, a microduck folded from a flat sheet, showing that shape-memory SEAs can be used to hold the 3D body configuration of a microrobot with no power consumption. Figure 5E shows a mechanical metamaterial, the canonical Miura-Ori pattern, with a negative Poisson ratio, a motif that has previously been used to demonstrate shape morphing structures and programmable metamaterials (*36*–*38*). Figure 5F shows an electrically addressable array of SEA hinges that can memorize an input signal. All of the designs in Fig. 5 are stable in both their flat state and their folded state without any external signals applied. These elements demonstrate the breadth of mechanically active shape-memory structures that can be created at the microscale with this technology.

DISCUSSION

Collectively, the properties of SEAs demonstrated here meet all the needs for voltage-controlled microscale shape-memory actuators in aqueous environments. They operate at low voltages (~1 V), respond quickly (~100 ms), achieve submicrometer radii (~500 nm) of curvature, and hold their positions for hours in the absence of applied voltages. These qualities make SEAs an excellent option for applications requiring ultrahigh-curvature shape-memory actuators in aqueous environments. Future work could include further increasing the working frequency and efficiency and designing all solid-state microactuators that work in air.

The demonstrated micro–shape memory actuators can be fabricated in parallel and are built with standard materials and photolithographic processing, leading to numerous potential applications. Their optical wavelength–sized radii of curvature could be harnessed to build nanophotonic devices such as mechanically reconfigurable optical metamaterials and metasurfaces (*39*, *40*) and adaptive topological photonics (*41*). By taking advantage of origami- and kirigami-based mechanisms, grippers and other manipulation devices could be designed for applications in microsurgery (*42*–*44*). Last, SEA standard fabrication protocols allow easy integration with microelectronic circuits and sensors, and their shape-memory operation allows them to function without continuously using power. These properties will be invaluable for the design and fabrication of microscopic robots.

MATERIALS AND METHODS

Fabrication of SEA devices

The fabrication process relies on growing Pt and TiO_2, etching these layers, fabricating polymeric panels, and finally releasing the resulting structures. (i) To fabricate the release layer, we sputtered 150-nm aluminum (doped with 1% silicon to create smaller, more uniform grains) on a borofloat glass. (ii) To protect this release layer during the etching and developing processes, we grew an additional 20 nm of Al_2O_3 using ALD at 110°C. Al_2O_3 is also etched by the developer but at a much slower rate. Therefore, it protects the Al during fabrication but can be removed in the final step by a prolonged exposure to the developer. (iii) To fabricate the devices, 2 nm of TiO_2 was grown onto the substrate using ALD. (iv) A positive photoresist was spin-coated, and the pattern was defined photolithographically. (v) The TiO_2 layer was etched by CF_4 at 150 W using inductively coupled plasma (ICP) etching (Oxford PlasmaLab 80+). (vi) Next, we grew 7 nm of Pt onto the TiO_2 using ALD. (vii) Next, a positive photoresist (Microposit S1813 for ABM contact aligner, UV40 for ASML 300C DUV stepper) was spin-coated, and the pattern was defined photolithographically. (viii) The Pt was then etched by an ion mill. We then removed the photoresist using an organic solvent. (ix) A second 2-nm layer of TiO_2 was grown onto the Pt using ALD. (x) A positive photoresist was spin-coated, and the pattern was defined by photolithography. (xi) The TiO_2 layer was etched by CF_4 at 150 W using ICP etching (Oxford PlasmaLab 80+), followed by Ar ICP etching (Oxford PlasmaLab 80+) at 30 W for 1 min. (xii) A negative photoresist (NLOF 2020 or SU8 2002) was spin-coated and patterned as the rigid panels. (xiii) Last, the devices were immersed in a basic developer AZ 726 MIF containing 2.38% tetramethylammonium hydroxide for several hours to etch the aluminum and Al_2O_3 sacrificial layers, thereby releasing the devices into the solution. The devices were then washed using deionized water several times and transferred into 1× PBS solution. We achieved a success rate greater than 95% for releasing and actuating devices like the ones shown in Figs. 1 (F to J) and 5. A schematic for the fabrication of a device with unidirectional folding is shown in fig. S2.

Alternate Ti capping layer

In some of the measurements and fabricated devices shown in Fig. 5, sputtered Ti was used as the capping layer, which produced a larger bending radius of 2 to 5 μm (figs. S8 and S9), allowing us to simplify the fabrication process and create larger structures that were easier to image in situ via optical microscopy. In such cases, we replace steps iii to v and ix to xi with the following processes: (i) A negative photoresist (NLOF 2020 or SU8 2002) was spin-coated and patterned. (ii) A 2-nm layer of Ti was sputtered onto the sample at 3 mTorr and 400 W. (iii) The sputtered Ti on top of the photoresist was lifted off in solvent.

Alternate SiO_2 rigid panels

To take the SEM images in Fig. 5, SiO_2 rigid panels were used instead of negative photoresist panels. The use of the SiO_2 panels prevents the distortion of the panels and delamination of Pt from the panels during critical point drying. In such cases, we fabricate SiO_2 panels after step ii using the following processes and skipped step xii. (i) A 500-nm-thick SiO_2 layer was deposited using plasma-enhanced chemical vapor deposition (Oxford 100). (ii) A positive photoresist (Microposit S1813) was spin-coated and patterned. (iii) The SiO_2 layer was etched by CHF_3/O_2 at 2500 W using ICP etching (Oxford PlasmaLab 100).

Electronic microscope imaging

High-resolution TEM imaging

The actuators were fabricated by depositing 70 cycles of Pt followed by 30 cycles of TiO_2 on a bare silicon wafer. An amorphous carbon layer (Sharpie marker) was smeared on top of the TiO_2 to protect samples during the subsequent procedure. To image the cross section of the Pt/TiO_2 bimorph using TEM, a thin cross-sectional lamina was milled from the top of the sample using an ion beam (Helios G4 UX FIB, Thermo Fisher Scientific). We then attached the sample to a copper TEM grid using a nanomanipulator. Last, the lamina was further thinned to electron transparency via a focused ion beam (FIB). The samples for in-plane TEM imaging were prepared by depositing 35, 45 (fig. S1), and 70 (Fig. 1) cycles of Pt on an 80-nm-thick silicon nitride membrane supported by silicon (from Greater Grids). The in-plane TEM imaging was performed in scanning TEM (STEM) mode on a probe-corrected TEM (Titan Themis Cryo S/TEM, Thermo Fisher Scientific) at 120 kV. The electron energy loss spectra (EELS) image and spectra for the cross section of the sample were collected using a Gatan Quefina dual-EELS spectrometer with 0.25 eV per channel.

Scanning electron microscopy imaging

To obtain the scanning electron microscopy (SEM) images of the devices (Figs. 1 and 5), the samples were released from the substrate and washed by deionized water and isopropanol sequentially. Then, the samples were dried in a critical point drier (Leica CPD300), sputtered with a thin layer of gold, and imaged in the SEM (Zeiss Supra 55).

Characterization of the electrochemical and mechanical properties of SEA devices

In situ characterization of both electrochemical and mechanical properties of SEA devices was performed in a custom-built two-electrode electrochemical cell on an inverted microscope (Olympus IX71) integrated with a three-axis micromanipulator (from Sensapex) and video camera. Each SEA device acted as the working electrode. Because the Ag/AgCl electrode is so large relative to the thin platinum surface that we are oxidizing, its potential remains constant. As such, this two-electrode electrochemical setup is just as good at measuring potential differences between the reference electrode and the working electrode when a microelectrode is used as the working electrode (*45*). Each device was lifted above the substrate using a micromanipulator with a PtIr probe coated with Parylene C so that only the few micrometers around the tip were exposed (Microprobes for Life Science). The reference electrode was a commercial flexible Ag/AgCl electrode in 3 M KCl (FLEX-REF, World Precision Instruments Inc.) with a low electrolyte leakage. The reference electrode also worked as a counter electrode because the surface area of the reference electrode is much larger than that of the platinum on the SEA devices. The cyclic voltammetry was measured using the following approach: A sweep voltage was generated via a data acquisition board controlled by a LabVIEW program, and the current was amplified through a current amplifier and collected by the same data acquisition board. These experiments were conducted in PBS (1×, pH 7.45). The memory time of the SEA devices was measured in both half-cell and full-cell configurations. For the half-cell configurations, the device was oxidized at different voltages for a specified duration and then was disconnected from the power supply. For the full-cell configurations, the potential of the device was set to a fixed value versus Ag/AgCl reference after the platinum was oxidized. Before the experiments, the cells were cleaned thoroughly with deionized water to remove all the adsorbed impurities. All the experiments were taken at 25°C. All the potential values in this study are specified relative to the Ag/AgCl/3 M KCl reference electrode used, which created a +210-mV shift relative to a standard hydrogen electrode. All the cyclic voltammetry data were taken at a sweep rate of 1 V/s. The electrochemical characterization and optical images were collected under the halogen lamp with red filter (600 to 650 nm) to avoid any photocatalytic effect of the TiO_2 layer. The optical images were taken by a monochromatic camera mounted on the microscope. As schematically shown in fig. S2I, the bending curvature κ was calculated on the basis of the length l and the bending angle θ of the hinge as $\kappa = \theta/l$. The bending angle θ of the hinge was calculated by measuring the projected area with respect to the actual area of the moving panel observed from the top in the microscope. The curvature was measured for different samples several tens of times, and they are consistent with the data reported here. Figure 3 shows representative data of the mechanical switching operations and electric properties, where the error is on the order of the symbol size.

Setup for measuring the conductivity

ALD platinum was deposited for 40 cycles to a thickness of about 5 nm on silicon dioxide cover slides. The resistivity of this platinum film is 2.5×10^{-7} (ohm·m), which is very close to the resistivity of the 70-cycle ALD platinum film (*6*) and only about 2.5 times of the resistivity of bulk platinum, indicating the formation of a continuous platinum film. Our previous results also show the ALD platinum grows into a continuous film above ~35 cycles (*10*). We photolithographically defined a pattern of long narrow platinum bars with an aspect ratio of 5 to 1 and etched the platinum via ion milling. We then sputtered thicker platinum contact pads. The samples were submerged in PBS solution (1×, pH 7.45). The conductivity of the thin platinum bars was measured using two PtIr electrodes coated with Parylene C so that only the few micrometers around the tip were exposed (Microprobes for Life Science). One side of the bar was biased at 50 mV, and the current through the bar was read with an Ithaco 1211 preamplifier and National Instruments DAQ. The potential between the platinum bar and the solution was set by the voltage applied to an Ag/AgCl electrode in the solution. More details on these measurements can be found in fig. S7. The conductivity was measured for different samples several times, and they are all consistent with the data reported here. These measurements of the electrochemically induced formation of the platinum oxide layer and the oxidation ratio are consistent with previous results from x-ray photoelectron spectroscopy (*26*, *46*, *47*). Figure 4 shows representative data of the electric properties, where the error is on the order of the symbol size.

SUPPLEMENTARY MATERIALS

robotics.sciencemag.org/cgi/content/full/6/52/eabe6663/DC1
Text SI. Analysis of the mechanical properties of SEA actuators.
Text SII. Calculation of the energy and power density.
Text SIII. Calculation of the thickness of platinum oxide layer.
Text SIV. Mechanical simulation of the SEA devices.
Fig. S1. TEM images of platinum membranes grown by ALD for different numbers of cycles.
Fig. S2. Fabrication process of a unidirectional SEA device.
Fig. S3. Statistical data for bending curvature versus applied voltage.
Fig. S4. Long time curvature measurement of the SEA after oxidation at 1.2 V for 2 s.
Fig. S5. By maintaining the SEA actuator in a full-cell configuration, one can apply a voltage to tune the memorized curvature.
Fig. S6. Electrical cycling stability of SEAs for 2000 cycles.
Fig. S7. In-plane conductance measurements of platinum thin films during oxidation.
Fig. S8. Cyclic voltammetry of a 2-nm-thick sputtered Ti layer.
Fig. S9. In situ characterization of the cyclic voltammetry and bending curvature versus applied voltage of a SEA actuator with Ti as the alternative inert layer in the OH^- (blue) and oxidation (yellow) regimes.
Fig. S10. Design of the kirigami/origami-based micromachines and microstructures.
Fig. S11. Simulation of the self-folding of the kirigami/origami-based micromachines and microstructures.
Table S1. Literature survey of the performance of voltage-driven planar actuators.
Table S2 Literature survey of additional important performance metrics of voltage-driven planar actuators.
Movie S1. Shape-memory effect in a gripper.
Movie S2. Electrical bending of Pt/TiO_2 and Pt/Ti SEA actuators.
Movie S3. Kirigami-based electrically programmable shape-memory micromachines.
Movie S4. Origami-based electrically programmable 3D microstructures.
References (*48*, *49*)

REFERENCES AND NOTES

1. J. M. Jani, M. Leary, A. Subic, M. A. Gibson, A review of shape memory alloy research, applications and opportunities. *Mater. Des.* **56**, 1078–1113 (2014).
2. R. Tickle, R. D. James, T. Shield, M. Wuttig, Y. Kadota, H. Hosaka, T. Morita, Shape memory piezoelectric actuator by control of the imprint electrical field. *Ferroelectrics* **368**, 185–193 (2008).

3. R. Tickle, R. D. James, T. Shield, M. Wuttig, V. V. Kokorin, Ferromagnetic shape memory in the NiMnGa system. *IEEE Trans. Magn.* **35**, 4301–4310 (1999).
4. A. Lendlein, H. Jiang, O. Jünger, R. Langer, Light-induced shape-memory polymers. *Nature* **434**, 879–882 (2005).
5. H. Meng, G. Li, A review of stimuli-responsive shape memory polymer composites. *Polymer* **54**, 2199–2221 (2013).
6. G. Welsch, R. Boyer, E. W. Collings, *Materials Properties Handbook: Titanium Alloys* (ASM International, 1994).
7. A. Lai, Z. Du, C. L. Gan, C. A. Schuh, Shape memory and superelastic ceramics at small scales. *Science* **341**, 1505–1508 (2013).
8. H. T. Lee, M. S. Kim, G. Y. Lee, C. S. Kim, S. H. Ahn, Shape memory alloy (SMA)-based microscale actuators with 60% deformation rate and 1.6 kHz actuation speed. *Small* **14**, 1801023 (2018).
9. M. S. Kim, H. T. Lee, S. H. Ahn, Laser controlled 65 micrometer long microrobot made of Ni-Ti shape memory alloy. *Adv. Mater. Technol.* **4**, 1900583 (2019).
10. M. Z. Miskin, A. J. Cortese, K. J. Dorsey, E. P. Esposito, M. F. Reynolds, Q. Liu, M. C. Cao, D. A. Muller, P. L. McEuen, I. Cohen, Electronically integrated, mass-manufactured, microscopic robots. *Nature* **584**, 557–561 (2020).
11. J. Weissmüller, R. N. Viswanath, D. Kramer, P. Zimmer, R. Würschum, H. Gleiter, Charge-induced reversible strain in a metal. *Science* **300**, 312–315 (2003).
12. K. Jung, J. Nam, H. Choi, Investigations on actuation characteristics of IPMC artificial muscle actuator. *Sens. Actuat. A Phys.* **107**, 183–192 (2003).
13. E. Smela, O. Inganäs, I. Lundström, Controlled folding of micrometer-size structures. *Science* **268**, 1735–1738 (1995).
14. X. Xia, A. Afshar, H. Yang, C. M. Portela, D. M. Kochmann, C. V. Di Leo, J. R. Greer, Electrochemically reconfigurable architected materials. *Nature* **573**, 205–213 (2019).
15. M. Z. Miskin, K. J. Dorsey, B. Bircan, Y. Han, D. A. Muller, P. L. McEuen, I. Cohen, Graphene-based bimorphs for micron-sized, autonomous origami machines. *Proc. Natl. Acad. Sci. U.S.A.* **115**, 466–470 (2018).
16. B. Bircan, M. Z. Miskin, R. J. Lang, M. C. Cao, K. J. Dorsey, M. G. Salim, W. Wang, D. A. Muller, P. L. McEuen, I. Cohen, Bidirectional self-folding with atomic layer deposition nanofilms for microscale origami. *Nano Lett.* **20**, 4850–4856 (2020).
17. G. Jerkiewicz, G. Vatankhah, J. Lessard, M. P. Soriaga, Y.-S. Park, Surface-oxide growth at platinum electrodes in aqueous H_2SO_4: Reexamination of its mechanism through combined cyclic-voltammetry, electrochemical quartz-crystal nanobalance, and Auger electron spectroscopy measurements. *Electrochim. Acta* **49**, 1451–1459 (2004).
18. S. Zeitler, E. Wendler-Kalsch, W. Preidel, V. Tegeder, Corrosion of platinum electrodes in phosphate buffered saline solution. *Mater. Corros.* **48**, 303–310 (1997).
19. L. B. Freund, J. A. Floro, E. Chason, Extensions of the Stoney formula for substrate curvature to configurations with thin substrates or large deformations. *Appl. Phys. Lett.* **74**, 1987–1989 (1999).
20. M. Fujihara, T. Kuwana, Studies of electrochemical interfaces of thin Pt film electrodes by surface conductance. *Electrochim. Acta* **20**, 565–573 (1975).
21. J. L. Tanner, D. Mousadakos, K. Giannakopoulos, E. Skotadis, D. Tsoukalas, High strain sensitivity controlled by the surface density of platinum nanoparticles. *Nanotechnology* **23**, 285501 (2012).
22. B. E. Conway, B. Barnett, H. Angerstein-Kozlowska, B. V. Tilak, A surface-electrochemical basis for the direct logarithmic growth law for initial stages of extension of anodic oxide films formed at noble metals. *J. Chem. Phys.* **93**, 8361–8373 (1990).
23. N. Cabrera, N. F. Mott, Theory of the oxidation of metals. *Rep. Prog. Phys.* **12**, 163–184 (1949).
24. H. A. Baroody, G. Jerkiewicz, M. H. Eikerling, Modelling oxide formation and growth on platinum. *J. Chem. Phys.* **146**, 144102 (2017).
25. S. A. Krasnikov, S. Murphy, N. Berdunov, A. P. McCoy, K. Radican, I. V. Shvets, Self-limited growth of triangular PtO_2 nanoclusters on the Pt (111) surface. *Nanotechnology* **21**, 335301 (2010).
26. M. A. van Spronsen, J. W. Frenken, I. M. Groot, Observing the oxidation of platinum. *Nat. Commun.* **8**, 429 (2017).
27. D. Rus, M. T. Tolley, Design, fabrication and control of origami robots. *Nat. Rev. Mater.* **3**, 101–112 (2018).
28. J. L. Silverberg, J. H. Na, A. A. Evans, B. Liu, T. C. Hull, C. D. Santangelo, R. J. Lang, R. C. Hayward, I. Cohen, Origami structures with a critical transition to bistability arising from hidden degrees of freedom. *Nat. Mater.* **14**, 389–393 (2015).
29. B. G. Chen, B. Liu, A. A. Evans, J. Paulose, I. Cohen, V. Vitelli, C. D. Santangelo, Topological mechanics of origami and kirigami. *Phys. Rev. Lett.* **116**, 135501 (2016).
30. J. L. Silverberg, A. A. Evans, L. McLeod, R. C. Hayward, T. Hull, C. D. Santangelo, I. Cohen, Using origami design principles to fold reprogrammable mechanical metamaterials. *Science* **345**, 647–650 (2014).
31. N. P. Bende, A. A. Evans, S. Innes-Gold, L. A. Marin, I. Cohen, R. C. Hayward, C. D. Santangelo, Geometrically controlled snapping transitions in shells with curved creases. *Proc. Natl. Acad. Sci. U.S.A.* **112**, 11175–11180 (2015).
32. L. Wang, J. Teng, P. Liu, A. Hirata, E. Ma, Z. Zhang, M. Chen, X. Han, Grain rotation mediated by grain boundary dislocations in nanocrystalline platinum. *Nat. Commun.* **5**, 4402 (2014).
33. L. Wang, P. Guan, J. Teng, P. Liu, D. Chen, W. Xie, D. Kong, S. Zhang, T. Zhu, Z. Zhang, E. Ma, New twinning route in face-centered cubic nanocrystalline metals. *Nat. Commun.* **8**, 2142 (2017).
34. X. Shu, D. Kong, Y. Lu, H. Long, S. Sun, X. Sha, H. Zhou, Y. Chen, S. Mao, Y. Liu, Size effect on the deformation mechanisms of nanocrystalline platinum thin films. *Sci. Rep.* **7**, 13264 (2017).
35. J. Li, B. Lu, H. Zhou, C. Tian, Y. Xian, G. Hu, R. Xia, Molecular dynamics simulation of mechanical properties of nanocrystalline platinum: Grain-size and temperature effects. *Phys. Lett. A* **383**, 1922–1928 (2019).
36. M. Schenk, S. D. Guest, Geometry of Miura-folded metamaterials. *Proc. Natl. Acad. Sci. U.S.A.* **110**, 3276–3281 (2013).
37. Z. Y. Wei, Z. V. Guo, L. Dudte, H. Y. Liang, L. Mahadevan, Geometric mechanics of periodic pleated origami. *Phys. Rev. Lett.* **110**, 215501 (2013).
38. L. Mahadevan, S. Rica, Self-organized origami. *Science* **307**, 1740 (2005).
39. J. Valentine, S. Zhang, T. Zentgraf, E. Ulin-Avila, D. A. Genov, G. Bartal, X. Zhang, Three-dimensional optical metamaterial with a negative refractive index. *Nature* **455**, 376–379 (2008).
40. Z. Liu, H. Du, J. Li, L. Lu, Z.-Y. Li, N. X. Fang, Nano-kirigami with giant optical chirality. *Sci. Adv.* **4**, eaat4436 (2018).
41. S. Barik, A. Karasahin, C. Flower, T. Cai, H. Miyake, W. DeGottardi, M. Hafezi, E. Waks, A topological quantum optics interface. *Science* **359**, 666–668 (2018).
42. K. Kim, X. Liu, Y. Zhang, J. Cheng, X. Y. Wu, Y. Sun, Elastic and viscoelastic characterization of microcapsules for drug delivery using a force-feedback MEMS microgripper. *Biomed. Microdevices* **11**, 421–427 (2009).
43. B. J. Edmondson, L. A. Bowen, C. L. Grames, S. P. Magleby, L. L. Howell, T. C. Bateman, Oriceps: Origami-inspired forceps, in *ASME 2013 Conference on Smart Materials, Adaptive Structures and Intelligent Systems* (ASME Digital Collection, 2013).
44. H. Suzuki, R. J. Wood, Origami-inspired miniature manipulator for teleoperated microsurgery. *Nat. Mach. Intell.* **2**, 437–446 (2020).
45. M. Lazerges, V. T. Tal, P. Bigey, D. Scherman, F. Bedioui, Electrochemical DNA-biosensors: Two-electrode setup well adapted for miniaturized devices. *Sens. Actuat. B Chem.* **182**, 510–513 (2013).
46. M. Peuckert, F. P. Coenen, H. P. Bonzel, XPS study of the electrochemical surface oxidation of Platinum in N H2SO4 acid electrolyte. *Electrochim. Acta* **29**, 1305–1314 (1984).
47. M. Peuckert, XPS investigation of surface oxidation layers on a platinum electrode in alkaline solution. *Electrochim. Acta* **29**, 1315–1320 (1984).
48. C. H. Hsueh, S. Lee, T. J. Chuang, An alternative method of solving multilayer bending problems. *J. Appl. Mech.* **70**, 151–154 (2003).
49. E. H. Sondheimer, The mean free path of electrons in metals. *Adv. Phys.* **50**, 499–537 (2010).

Acknowledgments: We thank N. L. Abbott, N. Bao, B. Bircan, K. Dorsey, T. Ma, T. Pearson, A. Cortese, Y. Ji, S. Norris, and Y. Yang for valuable discussions and T. Pennell, J. Clark, V. Genova, and G. Bordonaro for technical support. We thank R. Lang for the origami designs. **Funding:** This work was supported by the Army Research Office (ARO W911NF-18-1-0032), the National Science Foundation (EFMA-1935252), the Cornell Center for Materials Research (DMR-1719875), the Air Force Office of Scientific Research (MURI: FA9550-16-1-0031), and the Kavli Institute at Cornell for Nanoscale Science. This work was performed, in part, at Cornell NanoScale Facility, an NNCI member supported by NSF grant NNCI-2025233. **Author contributions:** Q.L., P.L.M., and I.C. conceived the experiments. Q.L. and W.W. designed and fabricated the SEAs, carried out the experiments, and collected and analyzed the data. M.F.R. collected and analyzed the data measuring oxide thickness. Q.L., W.W., M.F.R., and M.Z.M. developed the fabrication procedure of platinum actuator. M.C.C., Q.L., and D.A.M. conducted the electron microscopy imaging experiment. Q.L. and T.A. simulated the shape-memory effect. Q.L., I.C., and P.L.M. wrote the manuscript with all authors contributing. **Competing interests:** Q.L., M.Z.M., P.L.M., and I.C. are inventors on a patent application (63/087,056) submitted by Cornell University that covers electrically programmable microscale shape-memory actuators and related robotic devices. The other authors declare no competing interests. **Data and materials availability:** All data needed to evaluate the conclusions in the paper are present in the paper or the Supplementary Materials.

Submitted 6 September 2020
Accepted 18 February 2021
Published 17 March 2021
10.1126/scirobotics.abe6663

Citation: Q. Liu, W. Wang, M. F. Reynolds, M. C. Cao, M. Z. Miskin, T. A. Arias, D. A. Muller, P. L. McEuen, I. Cohen, Micrometer-sized electrically programmable shape-memory actuators for low-power microrobotics. *Sci. Robot.* **6**, eabe6663 (2021).

Science Robotics

Micrometer-sized electrically programmable shape-memory actuators for low-power microrobotics

Qingkun Liu, Wei Wang, Michael F. Reynolds, Michael C. Cao, Marc Z. Miskin, Tomas A. Arias, David A. Muller, Paul L. McEuen, and Itai Cohen

Sci. Robot. **6** (52), eabe6663. DOI: 10.1126/scirobotics.abe6663

Science Robotics (ISSN 2470-9476) is published by the American Association for the Advancement of Science. 1200 New York Avenue NW, Washington, DC 20005. The title *Science Robotics* is a registered trademark of AAAS.